Exact Torque and Force Model of Bearingless Electric Machines

Anvar Khamitov
Department of ECE
University of Wiconsin-Madison
Madison, WI 53706, USA
khamitov@wisc.edu

Eric L. Severson
Department of ECE
University of Wiconsin-Madison
Madison, WI 53706, USA
eric.severson@wisc.edu

***Abstract*—This paper proposes and develops a new and exact analytic electric machine model that has several potential advantages. The model can be used to address levitation performance requirements by developing exact force/torque regulation methods to precisely calculate commands to current regulators. This allows relaxing constraints during the design stage and has the potential to enable consideration of higher performance bearingless machines. Furthermore, analogous to torque enhancement in conventional electric machines, the proposed model can be used to identify options for suspension force enhancement by controlling multiple magnetic field harmonics. This paper provides a detailed derivation of the model and shows how it can be used to improve force regulation accuracy and enhance force density.**

***Index Terms*—Bearingless drive, bearingless motor, generalized Clarke transformation, multiphase winding, self-bearing motor**

I. Introduction

Bearingless motors have the potential to replace conventional motors with contact bearings and provide contact-free and lubricant-free support of the motor shaft [1]. However, their usage has been significantly limited by issues of low power density, efficiency, and high cost. Most bearingless motor prototypes reported in literature have been designed for low power ratings and relatively few machines have experimentally tested efficiencies of above 90%. Furthermore, they are not achieving the high speed-power capabilities that high performance conventional motors have [2]. All these limitations are because the design space of bearingless machines is significantly more constrained than conventional machines due to stringent levitation performance requirements. State-of-the-art models and force regulation algorithms are based on the assumption of a linear force/torque-current relationship that ignores the effects of magnetic field harmonics, saturation, or armature reaction. As a result, potentially high performance designs that do not fall under these simplified model assumptions can be excluded from consideration during design studies. Furthermore, the possibility of increasing force density using unmodeled airgap magnetic field harmonics is ignored.

This paper addresses the problem by proposing and developing an "exact" electric machine model that provides a new way of understanding force and torque creation. The proposed model is based on current space vectors to allow identification of current sequence components that excite specific magnetic field harmonics to increase force density. The paper shows how the exact model enables the creation of force/torque regulation techniques that can precisely actuate the shaft even when multiple airgap field harmonics are present. This allows relaxing the force vector error requirement during the design stage and addressing it during the control stage. As a result, this makes the design space less constrained and enables consideration of potentially higher performance designs. Only two studies, [3] and [4], have investigated techniques that can be referred to as exact force vector regulation. They demonstrated significant performance improvement for an active magnetic bearing (AMB) and a bearingless motor. However, the techniques they developed only work for specific machine examples and no generalized analytic model was presented.

The main contribution of this paper is to propose and develop a new and exact electric machine model that encompasses both force and torque creation, incorporating multiple airgap harmonics and stator winding interactions. Section II reviews airgap field theory that will be used in the model derivation. Sections III and IV review the textbook bearingless machine model typically used in literature, propose the exact model, and provide a detailed derivation from first principles using winding function theory, current sequences, and the Maxwell Stress Tensor. Section V compares the proposed model to the prior exact models in [3] and [4]. Sections VI and VII demonstrate benefits of using the proposed model for force ripple minimization and force enhancement.

II. Review of Airgap Field Theory

This section reviews the airgap field creation in bearingless electric machines as a special case of a more generalized multi-harmonic winding design study presented in [5]. The results summarized in (11)-(14) and (18) are used in Section IV to develop the exact model proposed by this paper. Sections II-A and II-B review magnetic field space harmonics using winding function theory and the relation to the current sequence components. Section II-C shows how to use the airgap fields to calculate the forces and torque using a reformulated form of the Maxwell Stress Tensor.

This work was supported in part by the USA National Science Foundation under Grant #1942099.

A. Harmonic Airgap Fields

This subsection reviews airgap magnetic field harmonics created by rotor magnets and stator winding currents. Winding function theory and circumferential current density are used to determine expressions for the winding fields.

The normal and tangential components of the airgap magnetic field (see Fig. 1b) are given by

$$B_{\text{n}} = B_{\delta} + B_{\text{n,w}}, \quad B_{\text{tan}} = B_{\text{tan,w}} \tag{1}$$

where B_{δ} is the rotor magnetic field, and $B_{\text{n,w}}$ and $B_{\text{tan,w}}$ are the winding's magnetic field components. The rotor magnetic field at harmonic h can be expressed in terms of the airgap angle α and the rotor angular position θ (defined in Fig. 1b):

$$B_{\delta,h} = \hat{B}_{\delta,h} \cos\left(h[\alpha - \theta]\right) \tag{2}$$

where $\hat{B}_{\delta,h=p} = \hat{B}_{\delta}$ is the magnetic loading. An example plot of $B_{\delta,h}$ along the airgap is illustrated in Fig. 1c.

The winding magnetic field depends on the winding layout and the phase currents. At space harmonic h:

$$B_{\text{n,w},h}(\alpha) = \tfrac{\mu_0}{\delta_{\text{eff}}} \sum_{k=1}^{m} N_{k,h}(\alpha) i_k, \;\; B_{\text{tan,w},h}(\alpha) = -\tfrac{\mu_0}{r} \sum_{k=1}^{m} A_{c,k,h}(\alpha) i_k \tag{3}$$

where δ_{eff} is the effective airgap length, i_k is the phase current in phase k, $N_{k,h}(\alpha)$ is the winding function [6] harmonic h of phase k, and $A_{c,k,h}(\alpha)$ is the circumferential current density per ampere of current. The winding function describes the distribution of the per ampere magnetomotive force:

$$N_{k,h}(\alpha) = \hat{N}_h \cos\left(h\alpha - \alpha_{\text{w0},h} - [k-1]h\alpha_{\text{ph,w}}\right) \tag{4}$$

where $\hat{N}_h = \frac{2}{\pi h} z_Q z_c \hat{k}_{w,h}$ and $\alpha_{\text{w0},h}$ are the winding function amplitude and phase shift at harmonic h. $\hat{N}_h$ is determined by the number of turns per coil z_Q, coils per phase z_c, and the winding factor $\hat{k}_{w,h}$. The angle $\alpha_{\text{ph,w}} = \frac{2\pi}{m s_{\Theta}}$ is the mechanical phase separation between adjacent phases, where s_{Θ} is introduced in [5] to develop a generalized winding design theory to independently create multiple airgap harmonics. The value of s_{Θ} can be any common divisor (CD) of the space harmonic orders $\{h_1, h_2, ...\}$ that the winding needs to create [5]. In separated windings, the value of s_{Θ} is typically p and p_s for torque and suspension windings, respectively. However, in combined windings, $s_{\Theta} = \text{CD}(p, p_s) = 1$.

Using the winding function, the per ampere circumferential current density $A_{c,k,h}(\alpha)$ at harmonic h can be calculated:

$$A_{c,k,h}(\alpha) = -\tfrac{\text{d}N_{k,h}(\alpha)}{\text{d}\alpha} = A'_{\text{c,ph},h} \sin\left(h\alpha - \alpha_{\text{w0},h} - [k-1]h\tfrac{2\pi}{m}\right) \tag{5}$$

where $A'_{\text{c,ph},h} = h\hat{N}_h = \frac{2}{\pi} z_Q z_c \hat{k}_{w,h}$. Substituting (4) and (5) into (3), the winding magnetic field components become:

$$\begin{aligned} B_{\text{n,w},h}(\alpha) &= \frac{\mu_0 \hat{N}_h}{\delta_{\text{eff}}} \sum_{k=1}^{m} i_k \cos\left(h\alpha - \alpha_{\text{w0},h} - [k-1]h\frac{2\pi}{m}\right) \\ B_{\text{tan,w},h}(\alpha) &= -\frac{\mu_0 h \hat{N}_h}{r} \sum_{k=1}^{m} i_k \sin\left(h\alpha - \alpha_{\text{w0},h} - [k-1]h\frac{2\pi}{m}\right) \end{aligned} \tag{6}$$

The phase currents i_k in (6) determine the behavior of the winding magnetic field at harmonic h when summed over all phases, resulting in counterclockwise (CCW) rotating, clockwise (CW) rotating, oscillating, or zero field. The following subsection provides more details about this relationship.

B. Field Relation to Sequence Currents

This subsection reviews the relation between the airgap fields and the phase currents. Current sequence components are defined and used to determine the field harmonics that they create in the airgap.

Any set of multiphase currents $\boldsymbol{i} = \begin{bmatrix} i_1 & i_2 & ... & i_m \end{bmatrix}^T$ can be decomposed into current sequence components as

$$\boldsymbol{i} = \boldsymbol{i_0} + \boldsymbol{i_1} + ... + \boldsymbol{i_s} + ... + \boldsymbol{i_{s_{\text{m}}}} \tag{7}$$

and the current at sequence s and phase order k is defined as

$$i_{s,k} = \hat{I}_s \cos\left(\phi_s - [k-1]s\frac{2\pi}{m}\right) \tag{8}$$

where each sequence s has an amplitude $\hat{I}_s$, a phase angle ϕ_s, and a phase separation $s\frac{2\pi}{m}$. The values of s can be

$$s = 0, \pm 1, ..., s_{\text{m}}, \text{ where } s_{\text{m}} = \begin{cases} \pm\frac{m-1}{2} & \text{for odd } m \\ \frac{m}{2} & \text{for even } m \end{cases} \tag{9}$$

The value of s is constrained between $-s_{\text{m}}$ and s_{m} because any other integer values outside this range result in the same phase separation angle $s\frac{2\pi}{m}$ due to the periodicity of 2π rad. The current sequences can be decoupled from each other by applying the GCT [7], [8]. As a result, each sequence component has an independent space vector representation. Space vectors for the sequences $s = 0$ and $s = m/2$ have 1-DOF (only real part) and a form of $\vec{i}_s = \hat{I}_s \cos\phi_s$. All other sequences have 2-DOF (real and imaginary parts) and a form of $\vec{i}_s = \hat{I}_s e^{\pm j\phi_s}$, with $+$ for $s > 0$ (positive sequence) and $-$ for $s < 0$ (negative sequence). This space vector representation of each sequence can be conveniently used to describe the magnetic field and force/torque creation.

Substituting (8) into (6) allows determining the magnetic field harmonics that are created due to a current sequence s (assuming that a winding factor $\hat{k}_{w,h} \neq 0$ at each harmonic). The terms inside the summation in (6) have the form of $\cos\left(\phi_s - [k-1]s\frac{2\pi}{m}\right)\cos\left(h\alpha - [k-1]h\frac{2\pi}{m}\right)$. For any values of s, h, and m, the summation in (6) is non-zero only if the phase separation angles $h\frac{2\pi}{m}$ and $s\frac{2\pi}{m}$ are equal:

$$h\frac{2\pi}{m} = \pm s\frac{2\pi}{m} + 2\pi b \tag{10}$$

where $2\pi b$ (b is an integer) indicates periodicity. Simplifying this equation shows that the sequence s can create the following airgap field harmonics:

$$h = \begin{cases} s + mb, & \text{for CCW rotating fields} \\ -s + mb, & \text{for CW rotating fields} \end{cases} \tag{11}$$

and the total magnetic field expression at these harmonics is

$$B_{\text{n,w},h}(\alpha) = \hat{B}_{\text{n,w},h}\cos\left(h\alpha - \alpha_{\text{w0,h}} \mp \phi_s\right)$$
$$B_{\text{tan,w},h}(\alpha) = -\hat{B}_{\text{tan,w},h}\sin\left(h\alpha - \alpha_{\text{w0,h}} \mp \phi_s\right) \quad (12)$$

where $-$ and $+$ signs indicate CCW or CW rotation. For example, a sequence $s = 2$ in $m = 5$ can create harmonics at $h = 2, 7, 12, ...$ rotating CCW and $h = 3, 8, 13, ...$ rotating CW. The magnetic field amplitudes in (12) are

$$\hat{B}_{\text{n,w},h} = \frac{m}{2}\frac{\mu_0 \hat{N}_h \hat{I}_s}{\delta_{\text{eff}}},\ \hat{B}_{\text{tan,w},h} = \frac{m}{2}\frac{\mu_0 h \hat{N}_h \hat{I}_s}{r} \quad (13)$$

When $s = 0$ or $s = m/2$, the magnetic field harmonics have an oscillating behavior (no rotation):

$$B_{\text{n,w},h} = 2\hat{B}_{\text{n,w},h}\left[\cos\left(h\alpha - \alpha_{\text{w0,h}} - \phi_s\right) + \cos\left(h\alpha - \alpha_{\text{w0,h}} + \phi_s\right)\right]$$
$$B_{\text{tan,w},h} = -2\hat{B}_{\text{tan,w},h}\left[\sin\left(h\alpha - \alpha_{\text{w0,h}} - \phi_s\right) + \sin\left(h\alpha - \alpha_{\text{w0,h}} + \phi_s\right)\right] \quad (14)$$

Equations (11)-(13) show that the current sequence s ($\hat{I}_s$ and ϕ_s) can be used to control the amplitude and angular location of the airgap magnetic field at harmonic h. Analogously, injecting multiple current sequences as in (7) allows controlling multiple airgap field harmonics. These results are used in the following section to develop the bearingless machine model.

C. Reformulation of the Maxwell Stress Tensor

Force and torque creation in electric machines directly depend on the airgap magnetic fields and can be described by the Maxwell Stress Tensor. This paper reformulates the standard Maxwell Stress Tensor formula in vector form as (15), which facilitates the derivation of the exact model:

$$\vec{F} = \frac{rL}{2\mu_0}\int_0^{2\pi} e^{j\alpha}\left[B_{\text{n}} + jB_{\text{tan}}\right]^2 \text{d}\alpha,\ \tau = \frac{r^2 L}{\mu_0}\int_0^{2\pi} B_{\text{n}}B_{\text{tan}}\text{d}\alpha \quad (15)$$

where $\vec{F} = F_x + jF_y$ is the force vector and τ is the torque, as shown in Fig. 1a. The parameters r and L are the rotor radius and axial length, B_{n} and B_{tan} are the normal and tangential components of the airgap magnetic field, and α is the airgap angle (see Fig. 1b). The airgap magnetic field consists of multiple space harmonics along α, each harmonic h having the form $\hat{B}_{\text{n/tan}}\cos(h\alpha \pm \phi_s)$, where ϕ_s is the angular location. This can be rewritten as $0.5\hat{B}_{\text{n/tan}}[e^{j(h\alpha\pm\phi_s)} + e^{-j(h\alpha\pm\phi_s)}]$ and used to solve (15) to identify harmonics that create force.

It is well-known that torque is created from the interaction between field harmonics of the same order h, while forces are created from the interaction between adjacent harmonics h and $h \pm 1$ [1]. This can be shown using (15). Suppose that the airgap field consists of two harmonics h_1 and $h_2 > h_1$:

$$B_{\text{n}} = \hat{B}_{\text{n},h_1}\cos(h_1\alpha - \phi_{s_1}) + \hat{B}_{\text{n},h_2}\cos(h_2\alpha - \phi_{s_2})$$
$$B_{\text{tan}} = -\hat{B}_{\text{tan},h_1}\sin(h_1\alpha - \phi_{s_1}) - \hat{B}_{\text{tan},h_2}\sin(h_2\alpha - \phi_{s_2}) \quad (16)$$

where ϕ_{s_1} and ϕ_{s_2} are the angular locations of these harmonics. By substituting these field expressions into the force equation in (15), it can be shown that the terms that result in non-zero integration have the form of (17) with $h_2 = h_1 + 1$:

$$\int_0^{2\pi} e^{j\alpha}\cos\left(h_1\alpha - \alpha_1\right)\cos\left(h_2\alpha - \alpha_2\right)\text{d}\alpha = \frac{\pi}{2}e^{j(\alpha_2 - \alpha_1)} \quad (17)$$

where α_1 and α_2 are the angles expressed in terms of ϕ_{s_1} and ϕ_{s_2}. This result is used multiple times when solving (15).

Solving (15) results in the following force expression:

$$\vec{F}_{h_1h_2} = \frac{V_r}{2\mu_0 r}\left(\hat{B}_{\text{n},h_1} - \hat{B}_{\text{tan},h_1}\right)\left(\hat{B}_{\text{n},h_2} + \hat{B}_{\text{tan},h_2}\right)e^{j(\phi_{s_2} - \phi_{s_1})} \quad (18)$$

Note that (18) is a general expression for force created by field harmonics h_1 and h_2. These fields can be from windings, magnets, or saliency. This result is used in the following sections to derive the textbook and exact models.

III. Textbook Model

This section provides an overview of the textbook model used in literature [1]. The derivation of the textbook model force/torque equations will be provided using the field calculations presented in Section II and its impact on machine design will be discussed.

A. Force/torque calculations

The textbook model assumes that the airgap field consists of only p and p_s pole pairs. Considering the fields from the magnets (2) and the windings (3), the total airgap magnetic field components have the form (the phase shift angle $\alpha_{\text{w0},p/p_s}$ is omitted for simplicity):

$$B_{\text{n}} = \hat{B}_\delta\cos\left(p[\alpha - \theta]\right) + \hat{B}_{\text{n,w},p}\cos(p\alpha - \phi_t) + \hat{B}_{\text{n,w},p_s}\cos(p_s\alpha - \phi_s) \quad (19)$$
$$B_{\text{tan}} = -\hat{B}_{\text{tan,w},p}\sin(p\alpha - \phi_t) - \hat{B}_{\text{tan,w},p_s}\sin(p_s\alpha - \phi_s)$$

where the subscripts t and s denote the torque and suspension current sequences used to excite p and p_s pole pairs.

The force vector expression can be derived using (18). When $h_1 = p$ or $h_2 = p$ is created by the magnets, $\hat{B}_{\text{n},h_1/h_2} = \hat{B}_\delta$, $\hat{B}_{\text{tan},h_1/h_2} = 0$, $\phi_{s_1}/\phi_{s_2} = \theta_e = p\theta$, and (18) simplifies to:

$$\vec{F} = \frac{V_r\hat{B}_\delta}{2\mu_0 r}\left(\hat{B}_{\text{n,w},p_s} \pm \hat{B}_{\text{tan,w},p_s}\right)e^{\pm j(\phi_s - \theta_e)}$$
$$\tau = \frac{V_r}{\mu_0}\hat{B}_\delta\hat{B}_{\text{tan,w},p}\sin(\phi_t - \theta_e) \quad (20)$$

where the $\pm$ signs correspond to $p_s = p \pm 1$. Note that the textbook model ignores the interaction between the stator p and p_s fields. Substituting (13) into (20), the force/torque expressions can be expressed in terms of the suspension and torque current space vectors as

$$\vec{F} = \bar{k}_f\vec{i}_s, \quad \vec{T} = \bar{k}_t\vec{i}_t \quad (21)$$

where the flux weakening component T_d is included in $\vec{T} = T_d + j\tau$. While $\vec{i}_s$ and $\vec{i}_t$ are calculated with the conventional CT for separated windings, [9] shows how this concept can be extended to multiphase (MP) and dual-purpose no voltage (DPNV) combined windings with the GCT. Parameters $\bar{k}_f$ and $\bar{k}_t$ are the per ampere force and torque

$$\bar{k}_f = \frac{\hat{B}_\delta V_r m p_s \hat{N}_{p_s}}{4r}\left(\frac{1}{p_s\delta_{\text{eff}}} \pm \frac{1}{r}\right)e^{\mp j\theta},\ \bar{k}_t = \frac{\hat{B}_\delta V_r m p \hat{N}_p}{2r}e^{-j\theta} \quad (22)$$

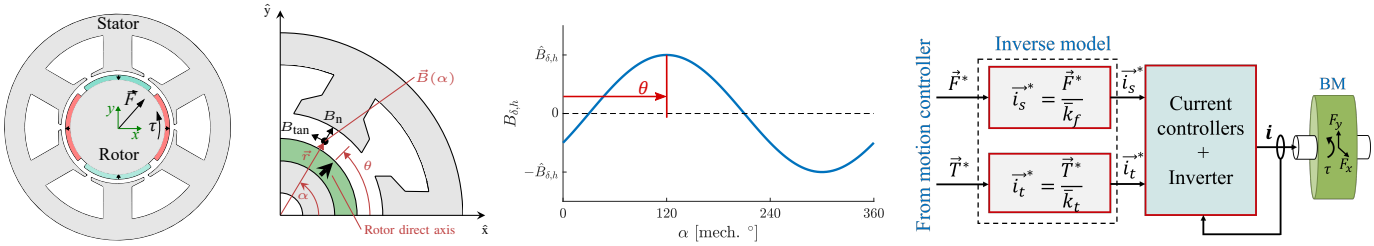

Fig. 1. (a) Force vector $\vec{F}$ and torque τ, (b) magnetic field components and angles (α and θ), (c) an example plot of the rotor magnetic field along the airgap at $h = 1$ for different θ, and (d) force/torque regulation block diagram.

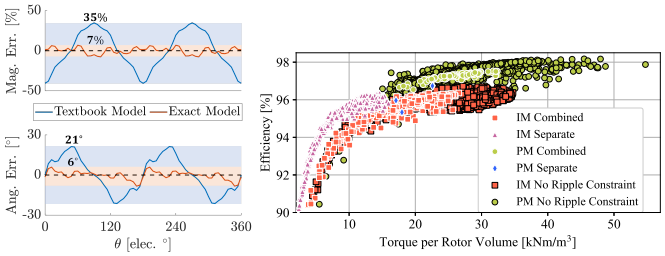

Fig. 2. (a) FEA results comparing textbook vs. exact models and (b) efficiency vs. torque density plot for 100 kW, 30 kRPM.

B. Discussion

The textbook model (21) is based on the dq control theory. The motor and suspension operation can be controlled in two independent space vector frames [8], [10] using the GCT and Park transformations. Desired phase currents are calculated by inverting the model (see Fig. 1d).

This model assumes perfectly sinusoidal airgap fields and its solution results in sinusoidal phase currents. The unmodeled magnetic field harmonics, armature reaction, and nonlinearities can cause large force vector error [1], [11]. This is shown in Fig. 2a where an example motor (described later in Fig. 3d) is commanded to create a x-axis force. However, the actual force obtained when phase currents are calculated using the textbook model has a large variation in the force vector magnitude and angle. This problem is typically solved in bearingless motor design studies by imposing the maximum error limits as constraints when sinusoidal phase currents are applied [12], [13]. However, this approach narrows the design space. Higher performance designs can be obtained if a more accurate machine model is used to determine the phase currents. Data from [2, Section III-E] has been replotted in Fig. 2b for permanent magnet (PM) and induction machines (IM) to demonstrate that 30% or more increase in torque density along with efficiency improvements up to 98% are possible when the force ripple constraint is removed.

IV. Proposed Exact Model

This section proposes the exact electric machine model, which is the main contribution of this paper. The model is applicable to all motor types, including PM, IM, and reluctance type motors. Section IV-A provides additional force calculations that are not considered in the textbook model (21). Based on this, Sections IV-B proposes the generalized exact model for bearingless machines, discusses its properties, and provides examples for different number of phases.

A. Additional terms in force calculation

As was previously mentioned, the suspension forces are created from the interaction between adjacent magnetic field space harmonics h and $h\pm1$. Based on this fact and (11)–(12), this paper identifies two additional force creation mechanisms that are not considered in the textbook model:

1) Forces from two adjacent current sequences. This can include the interaction between torque and suspension current sequences (armature reaction) or between other additional sequences that can be injected.
2) Forces from a single current sequence s_m (only occurs in machines with an odd number of phases m).

These two force creation mechanisms are now discussed. Analogous to the derivation in Section III-A, the force vector expression derived in (18) is used.

1) Force from two adjacent current sequences: Force can be created by applying two adjacent current sequences s_1 and $s_2 = s_1 + 1$, as (11) shows that this creates pairs of adjacent harmonics h_1 and $h_2 = h_1 + 1$ which rotate in the same direction (CCW or CW). The resulting airgap field and force are given by (16) and (18). Using (13), (18) can be expressed in terms of the current sequence components:

$$\vec{F}_{h_1h_2} = \bar{k}_{h_1h_2}\hat{I}_{s_1}\hat{I}_{s_2}e^{j(\phi_{s_2}-\phi_{s_1})} = \bar{k}_{h_1h_2}\vec{i}^{\,*}_{s_1}\vec{i}_{s_2} \tag{23}$$

$$\bar{k}_{h_1h_2} = \frac{\mu_0 V_r m^2 \hat{N}_{h_1}\hat{N}_{h_2}}{8r^2}\left(\frac{r}{\delta_{\mathrm{eff}}^2} - \frac{h_1h_2}{r} + \frac{1}{\delta_{\mathrm{eff}}}\right)e^{j(\alpha_{\mathrm{w0},h_2}-\alpha_{\mathrm{w0},h_1})}$$

2) Force from a single current sequence: Force can be created by injecting the highest current sequence $s_\mathrm{m} = \frac{m-1}{2}$ in odd phase windings. Equation (11) shows that this creates pairs of adjacent harmonics that rotate in opposite directions: for every integer value of $c \geq 0$, harmonics exist at $h_1 = s_\mathrm{m} + mc$ and $h_2 = -s_\mathrm{m} + m(c+1)$:

$$\begin{aligned} h_2 &= -s_\mathrm{m} + m(c+1) = -s_\mathrm{m} + mc + m - 1 + 1 \\ &= -s_\mathrm{m} + mc + 2s_\mathrm{m} + 1 = h_1 + 1 \end{aligned} \tag{24}$$

The created pairs of harmonics are $(s_\mathrm{m}, s_\mathrm{m}+1)$, $(s_\mathrm{m}+m, s_\mathrm{m}+m+1)$, $(s_\mathrm{m}+2m, s_\mathrm{m}+2m+1)$, ...

Similar to Section IV-A1, the total airgap magnetic field and the force vector due to these adjacent harmonics can be described by (16) and (18). However, since these harmonics rotate in opposite directions and are created by the same sequence s_m, their angular locations are $\phi_{s_1} = \phi_{s_\mathrm{m}}$, $\phi_{s_2} = -\phi_{s_\mathrm{m}}$ and their amplitudes depend on $\hat{I}_{s_\mathrm{m}}$, described by (13). This results in the following equation:

$$\vec{F}_{h_1h_2} = \bar{k}_{h_1h_2}\hat{I}^2_{s_\mathrm{m}} e^{-j2\phi_{s_\mathrm{m}}} = \bar{k}_{h_1h_2}\vec{i}^{*2}_{s_\mathrm{m}} \tag{25}$$

This equation shows that the single sequence s_m can be used to control the force vector magnitude $F_{h_1h_2} = \bar{k}_{h_1h_2}\hat{I}^2_{s_\mathrm{m}}$ and angle $\phi = -2\phi_{s_\mathrm{m}}$.

The quadratic force vector component in (25) is not considered in other bearingless motor literature publications which is surprising given that this force also appears in bearingless machines with three-phase windings. This includes all three-phase combined windings where $s = 0$ creates torque and $s = 1$ creates force, and all three-phase separated windings with $s_\Theta = 1$ (always true when $p = 1$ or $p_s = 1$). If these quadratic terms are not accounted for, conventional design processes attempt to minimize these terms (presumably through the use of large effective airgap lengths) as they create force vector error. Instead, if these new terms are handled in the force regulator, designers can enhance these terms to increase the suspension force capability.

B. Generalized exact force model

The total force acting on the rotor due to all harmonics is now summarized in a single model. This is calculated as the vector sum of the force due to each pair of adjacent field harmonics h_i and $h_j = h_i + 1$: $\vec{F} = \sum \vec{F}_{h_ih_j}$, where each force vector component $\vec{F}_{h_ih_j}$ is described by (18). Based on the force/torque derivations in Sections III-A and IV-A, three types of force components $\vec{F}_{h_ih_j}$ are identified that differ by their dependence on current space vectors:

- Textbook model: force from stator-rotor harmonic interactions. This term has a linear dependence on the current space vector and is summarized in (21).
- New term 1: force from stator-stator harmonic interactions where each harmonic is created by a unique current sequence. This term depends on the product of two current space vectors, see (23).
- New term 2: force from stator-stator harmonic interactions where both harmonics are created by the same current sequence. This term depends on the square of a single current space vector (25).

This paper proposes an exact force model that compiles the force terms created by all current space vectors that can be injected into the m-phase winding.

1) Matrix representation: The proposed model is written in matrix form as

$$\vec{F} = \vec{\boldsymbol{i}}^{\boldsymbol{T}}\bar{\boldsymbol{T}}_{\boldsymbol{Q}}\vec{\boldsymbol{i}} + \bar{\boldsymbol{T}}_{\boldsymbol{L}}\vec{\boldsymbol{i}} + \vec{F}_C \tag{26}$$

where $\vec{\boldsymbol{i}}$ is an $m\times 1$ array of the current space vectors and their conjugates calculated from the GCT matrix $\boldsymbol{C_m}$ as $\vec{\boldsymbol{i}} = \boldsymbol{C_m}\boldsymbol{i}$:

$$\vec{\boldsymbol{i}} = \begin{bmatrix}\vec{i}_0 & \vec{i}_1 & \vec{i}_2 & \dots & \vec{i}^*_2 & \vec{i}^*_1\end{bmatrix}^T \tag{27}$$

and $\bar{\boldsymbol{T}}_{\boldsymbol{Q}}$ and $\bar{\boldsymbol{T}}_{\boldsymbol{L}}$ are $m \times m$ and $1 \times m$ complex matrices that model the quadratic and linear dependencies of the force on the current space vectors, and $\vec{F}_C$ is the cogging force.

Every entry of $\bar{\boldsymbol{T}}_{\boldsymbol{Q}}$ is determined by (23) and represents the force per ampere squared created due to two current space vectors. This includes the forces due to two adjacent current space vectors as in (23) ($\vec{i}^*_1\vec{i}_2$, $\vec{i}^*_2\vec{i}_3$, ...) and due to the space vector s_m as in (25) ($\vec{i}^{*2}_{s_\mathrm{m}}$). Every entry of $\bar{\boldsymbol{T}}_{\boldsymbol{L}}$ is a force per ampere given in (22), which shows an interaction between adjacent rotor-stator field harmonics created by one current space vector ($\vec{i}_1$, $\vec{i}_2$, ...). Note that the $\vec{i}_t$ and $\vec{i}_s$ space vectors of the textbook model (21) are present in (27), but indicated as a sequence number; i.e. $\vec{i}_t = \vec{i}_1$ and $\vec{i}_s = \vec{i}_2$.

The proposed exact model in (26) can incorporate multiple harmonics by modifying $\bar{\boldsymbol{T}}_{\boldsymbol{Q}}$ and $\bar{\boldsymbol{T}}_{\boldsymbol{L}}$ matrix entries. Every entry of $\bar{\boldsymbol{T}}_{\boldsymbol{Q}}$ is a sum of the terms in (23) as $\bar{K}_{s_is_j} = \sum \bar{k}_{h_ih_j}$ for all adjacent airgap harmonics h_i and h_j created by the sequences s_i and $s_j = s_i + 1$ or the sequence s_m in odd phase machines. Similarly, every entry of $\bar{\boldsymbol{T}}_{\boldsymbol{L}}$ is the sum of the terms in (22) as $\bar{K}_{s_i} = \sum \bar{k}_{f,h_ih_r}$ for all adjacent harmonics h_i and h_r created by the sequence s_i and the rotor magnets. Depending on the relative rotation direction of these harmonics, some harmonic interactions result in a force ripple (having the $e^{j\pm 2\theta}$ term) or a constant force.

2) Space vector representation: Since only specific entries of $\bar{\boldsymbol{T}}_{\boldsymbol{Q}}$ are non-zero, the proposed model (26) can be rewritten using (21), (23), and (25) for even phase machines as:

$$\vec{F} = \sum_{i=1}^{s_\mathrm{m}-2} \bar{K}_{s_is_j}\vec{i}^*_{s_i}\vec{i}_{s_j} + \sum_{i=1}^{s_\mathrm{m}-1}\left(\bar{K}_{s_i}\vec{i}_i + \bar{K}_{s^*_i}\vec{i}^*_{s_i}\right) \tag{28}$$

and for odd phase machines as,

$$\vec{F} = \bar{K}_{s_\mathrm{m}s_\mathrm{m}}\vec{i}^{\,*}_{s_\mathrm{m}}{}^2 + \sum_{i=1}^{s_\mathrm{m}-1} \bar{K}_{s_is_j}\vec{i}^*_{s_i}\vec{i}_{s_j} + \sum_{i=1}^{s_\mathrm{m}}\left(\bar{K}_{s_i}\vec{i}_{s_i} + \bar{K}_{s^*_i}\vec{i}^*_{s_i}\right) \tag{29}$$

where $\vec{F}_C$ is omitted to save space. Note that odd phase machines have an additional term that depends on the space vector s_m due to (25). The term $\bar{K}_{s^*_i}\vec{i}^*_{s_i}$ is a force ripple term from interaction between adjacent magnet and winding field harmonics that rotate in opposite directions. Depending on the desired model accuracy, the coefficients in (28) and (29) can be modified to include the desired number of space harmonics.

3) Examples: To demonstrate the use of the proposed model, a force vector equation for an example nine-phase machine is now provided by expanding (29) (assuming that the rotor magnetic field is purely sinusoidal):

$$\vec{F}_{\text{9-ph}} = \bar{k}_{h_4h_5}\vec{i}^{*2}_4 + \bar{k}_{h_3h_4}\vec{i}^*_3\vec{i}_4 + \bar{k}_{h_2h_3}\vec{i}^*_2\vec{i}_3 + \bar{k}_{h_1h_2}\vec{i}^*_1\vec{i}_2 + \bar{k}_f\vec{i}_s \tag{30}$$

This machine has four independent rotating current space vectors. Here, $\bar{k}_f\vec{i}_s$ is the force from stator-rotor interaction

and $\vec{i}_s$ can be any space vector between $\vec{i}_1$ and $\vec{i}_4$ depending on p_s. Coefficients $\bar{k}_{h_1h_2}$, $\bar{k}_{h_2h_3}$, $\bar{k}_{h_3h_4}$, $\bar{k}_{h_4h_5}$ are the entries of $\bar{\boldsymbol{T}}_{\boldsymbol{Q}}$ and are calculated using (23). Differing from the textbook model (21), (30) shows that the proposed exact model has multiple quadratic terms. Accounting for these terms in a bearingless machine design study can potentially yield bearingless machine designs with enhanced force capability.

The proposed model (26) can be used to find the exact force vector expression for any m. As further examples, consider five- and six-phase machines, which have two rotating space vectors $\vec{i}_1$ and $\vec{i}_2$. When $\vec{i}_1 = \vec{i}_t$ and $\vec{i}_2 = \vec{i}_s$, force vector expressions can be obtained analogous to (30):

$$\vec{F}_{\text{5-ph}} = \bar{k}_q \vec{i}_s^{*2} + \bar{k}_{ft} \vec{i}_t^{*} \vec{i}_s + \bar{k}_f \vec{i}_s, \ \vec{F}_{\text{6-ph}} = \bar{k}_{ft} \vec{i}_t^{*} \vec{i}_s + \bar{k}_f \vec{i}_s \quad (31)$$

where $\bar{k}_q$ and $\bar{k}_{ft}$ are the entries of $\bar{\boldsymbol{T}}_{\boldsymbol{Q}}$ matrix in (26). As in (30), these equations have new quadratic terms due to two adjacent space vectors $\vec{i}_t^{*} \vec{i}_s$ and the highest space vector $\vec{i}_s^{*2}$ for $m = 5$. The $\vec{i}_s^{*2}$ term also appears in bearingless machines with three phases, as was discussed in Section IV-A2. To avoid force vector error created by these quadratic terms, (31) can be used to implement exact force vector regulation by analytically solving for phase current commands that eliminate force vector error, as demonstrated in Fig. 2a for a five-phase machine.

V. Comparison to Prior Exact Models

This section makes a comparison between the exact model developed in Section IV and the two studies [3] and [4] that developed the exact model for AMBs and bearingless motors, respectively. It will be shown that the models developed in these studies can be viewed as special cases of the exact model presented in Section IV.

A. Exact AMB Model

Study [3] developed the exact force vector model for a three-pole ($m = 3$) AMB, as shown in Fig. 3a, where the radial forces are created due to bias and control fields. Using this model, [3] proposed an analytic framework to find the desired coil currents (equivalent to solving a quartic polynomial equation) and experimentally demonstrated the performance improvement using the proposed exact force vector regulator compared to the conventional regulation approaches.

The exact force vector model in [3, eq. (19)-(20)] can be rewritten using the notation in this paper as

$$\vec{F}_{\text{AMB}} = \frac{3}{2} k_1 \left(\frac{1}{2} \left(\hat{B}_{\text{n,w,1}} e^{-j\phi_1} \right)^2 + 2 B_{\delta,0} \hat{B}_{\text{n,w,1}} e^{j\phi_1} \right) \quad (32)$$

where $B_{\delta,0}$ is a homopolar magnetizing field, $\hat{B}_{\text{n,w,1}}$ is the amplitude of a rotating two-pole field described by (12), and k_1 is a constant that represents the force-field relationship. The rotating field is created by three-phase currents ($s = 1$) represented by $\vec{i}_1 = \hat{I}_1 e^{j\phi_1}$. When the constants are combined together, (32) can be rewritten as

$$\vec{F}_{\text{AMB}} = \bar{k}_q \vec{i}_1^{*2} + \bar{k}_f \vec{i}_1 \quad (33)$$

which shows the force vector has both quadratic and linear dependencies on the currents. The newly proposed exact model (26) can be simplified to (33) for this machine (three-phase winding, $s = s_{\text{m}} = 1$ creates force, $s = 0$ could create torque).

B. Exact Bearingless Flux-Switching Motor Model

Study [4] presented the exact force/torque motor model for bearingless machines. The model considers the linear (stator-rotor interactions) and quadratic (stator-stator interactions) dependence of the force/torque on the phase currents. Although the model in [4] was shown to improve force vector regulation accuracy, [4] assumed that the force components from the phase-to-phase interactions ($i_1 i_2$, $i_2 i_3$, ...) are negligible. This assumption limits the use of the model to a specific motor topology such as the flux-switching motor with flux barriers that was used for the case study in [4] (see Fig. 3b). Furthermore, the model is FEA-based and no analytic expressions were developed, which makes it difficult to understand the actual physics of the machine and its system properties.

Unlike the exact model (26) developed in this paper, the model in [4, eq. (1)] is based on phase current quantities:

$$\begin{aligned} \vec{F} &= \boldsymbol{i}^{\boldsymbol{T}} \bar{\boldsymbol{T}}_{\boldsymbol{Q},\boldsymbol{xy}} \boldsymbol{i} + \bar{\boldsymbol{T}}_{\boldsymbol{L},\boldsymbol{xy}} \boldsymbol{i} + \bar{T}_{C,xy} \\ \tau &= \boldsymbol{T}_{\boldsymbol{L},\boldsymbol{\tau}} \boldsymbol{i} + T_{C,\tau} \end{aligned} \quad (34)$$

where $\boldsymbol{i} = \begin{bmatrix} i_1 & i_2 & ... & i_m \end{bmatrix}^T$ is an array of the phase currents. $\bar{\boldsymbol{T}}_{\boldsymbol{Q},\boldsymbol{xy}} = \boldsymbol{T}_{\boldsymbol{Q},\boldsymbol{x}} + j\boldsymbol{T}_{\boldsymbol{Q},\boldsymbol{y}}$ is $m \times m$ matrix that represents quadratic dependence; $\bar{\boldsymbol{T}}_{\boldsymbol{L},\boldsymbol{xy}} = \boldsymbol{T}_{\boldsymbol{L},\boldsymbol{x}} + j\boldsymbol{T}_{\boldsymbol{L},\boldsymbol{y}}$ and $\boldsymbol{T}_{\boldsymbol{L},\boldsymbol{\tau}}$ are $1 \times m$ matrices that represent linear dependence; $\bar{T}_{C,xy} = T_{C,x} + j_{C,y}$ and $T_{C,\tau}$ are the terms that represent cogging forces/torque (no dependence on currents). Since phase-to-phase interactions were ignored, [4] set the non-diagonal entries of $\bar{\boldsymbol{T}}_{\boldsymbol{Q},\boldsymbol{xy}}$ to zero and rewrote the quadratic term as $\boldsymbol{i}^{\boldsymbol{T}} \bar{\boldsymbol{T}}_{\boldsymbol{Q},\boldsymbol{xy}} \boldsymbol{i} = \text{diag}\left(\bar{\boldsymbol{T}}_{\boldsymbol{Q},\boldsymbol{xy}}\right)(\boldsymbol{i} \circ \boldsymbol{i})$. Here, $\boldsymbol{i} \circ \boldsymbol{i} = \begin{bmatrix} i_1^2 & i_2^2 & ... i_m^2 \end{bmatrix}^T$ is the Hadamard product.

The exact model proposed by this paper includes all phase current interactions through space vector currents. Therefore, the model in [4] is a special case of the exact model in (26). Using the space vector transformation $\vec{\boldsymbol{i}} = \boldsymbol{C}_{\boldsymbol{m}} \boldsymbol{i}$, the relationship between the matrices in (26) and (34) is determined:

$$\bar{\boldsymbol{T}}_{\boldsymbol{Q},\boldsymbol{xy}} = \boldsymbol{C}_{\boldsymbol{m}}^{\boldsymbol{T}} \bar{\boldsymbol{T}}_{\boldsymbol{Q}} \boldsymbol{C}_{\boldsymbol{m}}, \quad \bar{\boldsymbol{T}}_{\boldsymbol{L},\boldsymbol{xy}} = \bar{\boldsymbol{T}}_{\boldsymbol{L}} \boldsymbol{C}_{\boldsymbol{m}} \quad (35)$$

VI. Force Ripple Minimization

This section shows how the proposed exact model can be used to minimize force ripple. Simulation results using two example five-phase machines are presented.

The force ripple in literature is typically characterized by force magnitude error E_m and force angle error E_a [14]. This is illustrated in Fig. 3c, where the desired force $\vec{F}^*$ is along x-axis, while the actual force $\vec{F}$ can have both F_x and F_y components at any rotor angular position. These two metrics are calculated as $E_m = \frac{F_{\text{max}} - F_x}{F_x}$ and $E_a = \tan^{-1}\left(\frac{F_y}{F_x}\right)$, which show the maximum deviation from the desired force magnitude and angle. Study [1] reported large force angle error ($> 17^\circ$) can cause instability in suspension regulation and [15] suggested to keep force angle error below $< 5^\circ$.

The two examples used to demonstrate the benefits of the proposed exact model are a five-phase SPM (Fig. 3d) and

TABLE I
EXAMPLE MOTOR PARAMETERS

	SPM	IM		SPM	IM
$\bar{k}_f$ (N/A)	$6.46e^{-j\theta}$	0	Outer radius (mm)	200	
$\bar{k}_{ft}$ (N/A^2)	2.84	10.6	Rated speed (kRPM)	30	
$\bar{k}_q$ (N/A^2)	-0.58	-1.92	Rated P_{out} (kW)	9.8	

IM (Fig. 3e) machine that have the same stator. The key parameters are given in Table I, including the quadratic force coefficients of (31). Figure 2a compares the error in force vector magnitude and angle for the SPM example when the textbook (21) and the exact (31) models are used to solve for the phase currents to create a force $F_x = 20$ N. For the exact model, solving (31) for the phase currents is equivalent to solving a fourth order polynomial equation, which has up to four real solutions. The solution with the lowest ohmic losses $\sum_{k=1}^{5} i_k^2$ is selected (Euclidean L^2 norm). Cogging force is not included and linear iron material is used. Figure 2a shows that the exact model can significantly improve force actuation accuracy. Figure 3f shows the polar plot of force vector components in (31) for the IM example when the rated suspension current space vector $\vec{i}_s$ is applied and rotated over 360 degrees. This plot shows the significance of the quadratic $\bar{k}_q$ term on the total force created on a shaft.

The proposed exact model can also be used to minimize the force ripple during the design stage. If the designer desires to eliminate the effects of the quadratic term $\bar{k}_q \vec{i}_s^{*2}$, it can be shown using (23) that this can happen when the machine design parameters are selected to have the relation $p_s \delta_{\text{eff}} = r$. This can be advantageous for machines with a small rotor radius or a high number of pole pairs.

VII. FORCE ENHANCEMENT

This section demonstrates the benefits of using the proposed model to analyze different phase windings and force enhancement options. Three bearingless machines with $m = 5$, 6, and 8 are compared over a range of magnetizing field $\hat{B}_\delta$. All examples have $p = 1$, the same motor dimensions, and the same total number of turns $mz_Q z_c$ to allow a comparison in per-unit [p.u.] quantities. The force vector models for five and six phases are given in (31) and the force vector model for eight phases is similar to (30), but without the $\bar{k}_{h_4 h_5} \vec{i}_4^{*2}$ term.

First, the machines are compared in terms of their rated force capabilities without exceeding a maximum allowable airgap field $\max(|B(\alpha)|) \leq B_{\max} = 1$ p.u. The rated force is obtained by generating the maximum force profile, as shown in Fig. 4a, and drawing the inner contour (shown as an inscribed red dashed circle for $\hat{B}_\delta = 0.5$ p.u.). Based on this, the rated force vs. $\hat{B}_\delta$ is obtained and plotted in Fig. 4b (top subplot). Figure 4a illustrates that, unlike $m = 6$ and 8, the $m = 5$ machine has non-convex maximum force profiles for a range of $\hat{B}_\delta$ values. This results in F_{rated} being a non-convex function of $\hat{B}_\delta$, as shown in Fig. 4b (two maxima at $\hat{B}_\delta = 0$ and 0.7 p.u.). This is due to the quadratic term in (31), which also appears in certain three-phase separated windings and three-pole AMBs [3], as described in Section V-A.

Figure 4b also compares the current rating and the average ohmic losses per unit of the rated force (subplots 1 and 2). These results show that the eight-phase machine can create the largest force for all values of $\hat{B}_\delta$ because of being able to independently create three rotating harmonics that create forces. At $\hat{B}_\delta \leq 0.2$ p.u., $m = 5$ and 8 have more desirable performance than $m = 6$ in all metrics. This is particularly true for $m = 5$ at $\hat{B}_\delta = 0$ because 0.9 p.u. of force can be created with the quadratic term in (31), resulting in the lowest current rating and ohmic losses. At $0.3 < \hat{B}_\delta \leq 0.7$ p.u., $m = 6$ and 8 machines have a similar and favorable performance which exceeds the $m = 5$ machine. At $\hat{B}_\delta \geq 0.7$ p.u., the $m = 8$ machine has the highest force, albeit with the largest current and losses.

The machines are also compared in terms of their torque capabilities. In this comparison, the motor creates a constant force (equal to the rotor weight W_r or its multiple) and the torque that the motor can create at any force angle without exceeding the maximum airgap field limit is determined. Figure 4c shows that the torque performance in $m = 6$ and 8 is the same in all cases, with a peak torque at $\hat{B}_\delta = 1/\sqrt{2}$. The torque performance of the $m = 5$ machine is poorer, which is especially noticeable at high force values.

The results in this section show that the motor's magnetizing field has a strong influence on which number of phases is most desirable. For machines with low $\hat{B}_\delta$ (low torque), windings having quadratic forces (25) can be more advantageous, as was demonstrated for $m = 5$. For machines with larger $\hat{B}_\delta$ or variable $\hat{B}_\delta$ values, machines with larger m may be the best option due to the ability to create additional force components.

VIII. CONCLUSION

This paper proposes an exact force/torque model for bearingless electric machines using current space vector/sequence components and their relationship to airgap magnetic field space harmonics. It is found that previous attempts at developing the exact models for magnetic bearings and bearingless motors can be viewed as special cases of the generalized model developed in this paper. Furthermore, the paper finds that all three-phase combined windings and some three-phase separated windings have quadratic force vector components, which have been neglected in previous literature. The paper finds that when these terms are ignored in the force model, substantial force vector error can result; however, when properly handled, these additional forces can increase the machine's force rating, particularly at low magnetizing field values.

The proposed model is applicable to all motor types, is analytic-based, and captures the underlying physics of the machine accurately. These features equip the machine and controls designers with tools to increase the torque and levitation system performance. The paper finds that the developed model can be used to eliminate the force vector error by selecting a certain combination of machine design parameters during the design stage or by having the control system analytically solve the exact model during runtime to determine phase currents as the sum of multiple current sequences. The paper

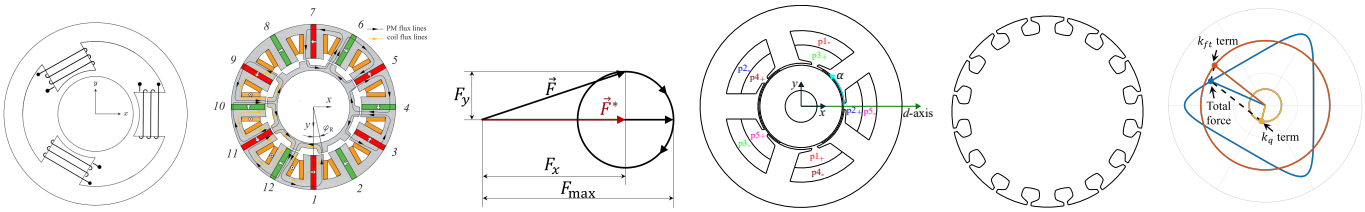

(a) (b) (c) (d) (e) (f)

Fig. 3. (a) and (b) electric machine cross-sections used in the development of the exact models for three-pole AMB in [3] and bearingless flux-switching motor in [4], rexpectively, (c) illustration of force magnitude and angle error. SPM and IM examples with the same stator $Q = 5$ and $m = 5$: (d) SPM example cross-section, (e) IM example rotor cross-section, and (f) polar plot of force vector components for the IM example.

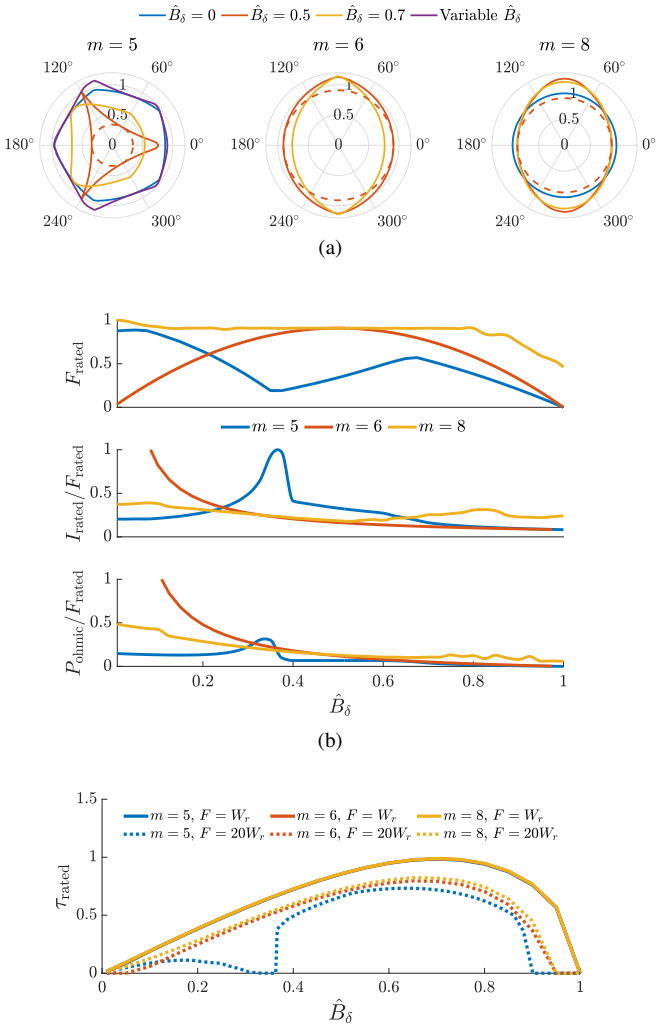

(a)

(b)

(c)

Fig. 4. Comparison between $m = 5$-, 6-, and 7-phase bearingless machines. All dimensions are in p.u.: (a) maximum force profiles shown for different magnetizing fields, (b) force rating, current rating, and average ohmic losses vs. $\hat{B}_\delta$, and (c) torque rating vs. $\hat{B}_\delta$ for different force magnitudes.

finds that increasing the number of phases can enhance force creation over a wide range of magnetizing field values, while maintaining favorable current ratings and ohmic losses.

In conclusion, the findings of this paper provide motivation to rethink the design approach of bearingless machines to include additional force creation mechanisms and to develop regulation techniques that use the proposed exact model. These developments have potential to make the design space of bearingless machines less constrained and enable consideration of higher performance designs.

References

[1] A. Chiba, T. Fukao, O. Ichikawa, M. Oshima, M. Takemoto, and D. Dorrell, *Magnetic Bearings and Bearingless Drives*. Newnes, 2005.

[2] J. Chen, J. Zhu, and E. L. Severson, "Review of bearingless motor technology for significant power applications," *IEEE Transactions on Industry Applications*, vol. 56, no. 2, pp. 1377–1388, 2020.

[3] N. R. Hemenway and E. L. Severson, "Three-pole magnetic bearing design and actuation," *IEEE Transactions on Industry Applications*, vol. 56, no. 6, pp. 6348–6359, 2020.

[4] N. Turk, N. Bulić, and W. Gruber, "Nonlinear control of a bearingless flux-switching slice motor with combined winding system," *IEEE/ASME Transactions on Mechatronics*, vol. 25, no. 1, pp. 152–163, 2020.

[5] F. Nishanth, A. Khamitov, and E. L. Severson, "Design of multiphase motor windings for control of multiple airgap fields," in *2022 IEEE Energy Conversion Congress and Exposition (ECCE)*.

[6] T. A. Lipo, *Analysis of synchronous machines*. Crc Press, 2017.

[7] A. Wilamowski and M. Bogdan, "The industrial electronics handbook power electronics," *Taylor and Francis Group*, 2011.

[8] G. Grandi, G. Serra, and A. Tani, "General analysis of multi-phase systems based on space vector approach," in *2006 12th International Power Electronics and Motion Control Conference*. IEEE, 2006, pp. 834–840.

[9] A. Khamitov, W. Gruber, G. Bramerdorfer, and E. L. Severson, "Comparison of combined winding strategies for radial nonsalient bearingless machines," *IEEE Transactions on Industry Applications*, vol. 57, no. 6, pp. 6856–6869, 2021.

[10] W. Gruber and S. Silber, "Dual field-oriented control of bearingless motors with combined winding system," in *2018 International Power Electronics Conference (IPEC-Niigata 2018 -ECCE Asia)*, May 2018, pp. 4028–4033.

[11] T. Schneider, J. Petersen, and A. Binder, "Influence of pole pair combinations on high-speed bearingless permanent magnet motor," 2008.

[12] A. Farhan, M. Johnson, K. Hanson, and E. L. Severson, "Design of an ultra-high speed bearingless motor for significant rated power," in *2020 IEEE Energy Conversion Congress and Exposition (ECCE)*, 2020, pp. 246–253.

[13] J. Chen, A. Farhan, M. Johnson, and E. L. Severson, "Design of bearingless permanent magnet motors using no voltage combinedwindings," in *The 10th International Conference on Power Electronics, Machines and Drives (PEMD 2020)*, vol. 2020, 2020, pp. 803–808.

[14] Y. g. Kang and E. L. Severson, "Optimization framework for a large, high speed bearingless permanent magnet motor," in *Sixteenth International Symposium on Magnetic Bearings*, August 2018, pp. 1–10.

[15] R. P. Jastrzebski, P. Jaatinen, O. Pyrhönen, and A. Chiba, "Design of 6-slot inset pm bearingless motor for high-speed and higher than 100kw applications," in *Electric Machines and Drives Conference (IEMDC), 2017 IEEE International*. IEEE, 2017, pp. 1–6.